ChemPubSoc Europe
DOI: 10.1002/chem.201603678
CHEMISTRY
A European Journal
Full Paper

Liquid Crystals

Effect of Atomic-Scale Differences on the Self-Assembly of Thiophene-based Polycatenars in Liquid Crystalline and Organogel States

Balaram Pradhan,[a] V. M. Vaisakh,[b] Geetha G. Nair,[b] D. S. Shankar Rao,[b] S. Krishna Prasad,[b] and Achalkumar Ammathnadu Sudhakar*[a]

Dedicated to Professor Takuzo Aida

Abstract: Two series of polycatenars are reported that contain a central thiophene moiety connected to two substituted oxadiazole or thiadiazole units. The number, position, and length of the peripheral chains connected to these molecules were varied. The oxadiazole-based polycatenars exhibited columnar phases with rectangular and hexagonal or oblique symmetry, whereas the thiadiazole-based polycatenars exhibited columnar phases with rectangular and/or hexagonal symmetry. All of the compounds exhibited bright emission in the solution and thin-film states. Two oxadiazole-based molecules and one thiadiazole-based molecule exhibited supergelation ability in hydrocarbon solvents, which is mainly supported by attractive π–π interactions. These gels showed aggregation-induced enhanced emission, which is of high technological importance for applications in solid-state emissive displays. X-ray diffraction studies of the xerogel fibers of oxadiazole-based polycatenars revealed a columnar rectangular organization, whereas a hexagonal columnar arrangement was observed for thiadiazole-based polycatenars. Rheological measurements carried out on the samples quantitatively confirmed the formation of gels and showed that these gels are mechanically robust. The impact of an atomic-scale difference (oxygen to sulfur, $<2\%$ of the molecular weight) on the self-assembly and the macroscopic properties of those self-assembled structures are clearly visualized.

Introduction

Thiophene-based molecular materials are an extensively studied type of heterocyclic materials because of their synthetic flexibility and applications as p-type (electron-rich) semiconductor systems.[1] Thiophene-based oligomers and polymers are known for their unique optoelectronic properties and have found utility in the fabrication of field-effect transistors,[2] light-emitting diodes,[3] and photovoltaic cells.[4] Most oligothiophenes must be purified by vacuum-sublimation techniques due to their poor solubility. Thus, liquid-crystalline (LC) thiophene derivatives seem to be good alternatives due to their good solubility because of which they can be easily purified. Furthermore, good-quality thin films can be obtained by simple solution-processing techniques and further molecular alignment can be addressed through annealing. Most of the thiophene-based liquid crystals reported stabilize nematic and smectic phases.[5] A few oligomers with a higher number of flexible terminal tails were reported to stabilize columnar (Col) phases.[6] Stabilization of Col phases in this class of materials is beneficial because the stacking of molecules one above the other to form columns of indefinite length provides a pathway for one-dimensional charge migration. As mentioned earlier, the ease of processability makes the Col phase an ideal substitute for conjugated polymers or organic single crystals from the viewpoint of optoelectronic devices.[7] π-Conjugated molecules that contain strong donor (D) and acceptor (A) systems show intramolecular charge transfer and low bandgap properties, which make them attractive.[8] Kato et al. reported star-shaped molecules containing three donor thiophene moieties connected to a central electron-accepting triazine moiety, which exhibited a Col phase with ambipolar conductivity.[6b] 1,3,4-Oxadiazole derivatives, which are known for their electron-deficient and fluorescence nature, are finding applications in OLEDs as electron transport and electroluminescent layers.[9] These have been integrated into the liquid-crystal design to obtain conductive smectic or columnar mesophases.[10] 1,3,4-Thiadiazole derivatives are less often reported, but they also exhibit promising thermal and photophysical behavior.[11] The self-assembly of thiophene-based molecules into organogels has been studied extensively because of the enhanced charge-transport behavior and optoelectronic properties due to molecular packing in the self-assembled systems.[3a,12] In most

---

[a] B. Pradhan, Dr. A. A. Sudhakar
Department of Chemistry, Indian Institute of Technology Guwahati
Guwahati, 781039, Assam (India)
E-mail: achalkumar@iitg.ernet.in

[b] V. M. Vaisakh, Dr. G. G. Nair, Dr. D. S. S. Rao, Dr. S. K. Prasad
Centre for Nano and Soft Matter Sciences
Bangalore (India)

Supporting information for this article, including color images, is available on the WWW under http://dx.doi.org/10.1002/chem.201603678.

cases, such self-assembled systems are assisted by intermolecular hydrogen bonding augmented by peptide or amide units. Recently, a few liquid crystalline polycatenars with 1,3,4-oxadiazole units have exhibited gelation, which is exclusively supported by π–π interactions.[13] However, there are no reports on thiophene-containing organogels, which are stabilized mainly by π–π interactions. Tailoring the molecular structure to obtain these long-range-ordered self-assembled structures is important, given their potential applications in optoelectronic devices.

Considering all these aspects, we aspired to design a new polycatenar system that contains a central electron-rich thiophene unit connected to two electron-deficient fluorophores, such as substituted 1,3,4-oxadiazole or 1,3,4-thiadiazole units. We expected that these compounds would show good luminescence, thermal behavior, and ability to undergo organogelation. The alternate arrangement of donor and acceptor moieties may modulate the bandgap of these molecules. We envisaged that the presence of oxadiazole and thiadiazole could result in a drastic difference in the self-assembly and related macroscopic properties. The number of flexible chains, their positions, and their length were modified to understand the impact on the self-assembly and photophysical properties of these polycatenar systems.

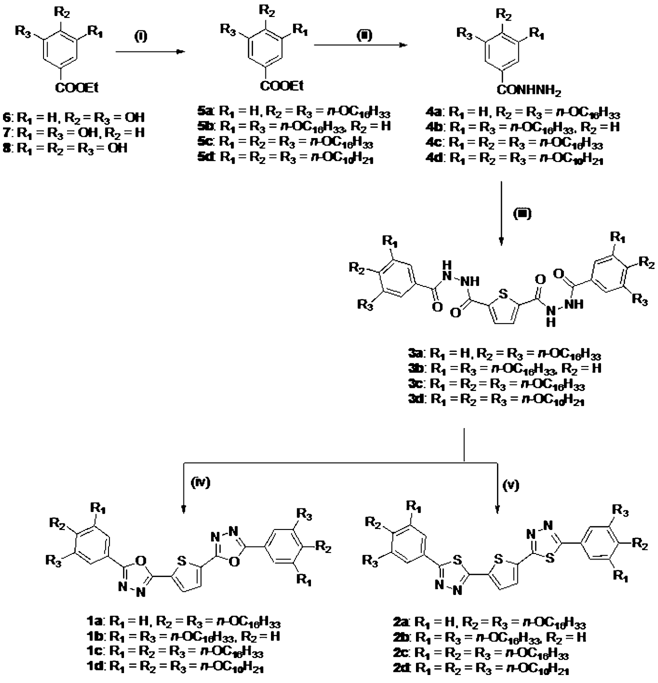

Scheme 1. Reagents and conditions: i) *n*-Bromoalkanes, anhydrous K_2CO_3, DMF, 80 °C, 24 h (70–80 %); ii) $NH_2NH_2{\cdot}H_2O$, ethanol or butanol, reflux, 48 h (70–80 %); iii) thiophene-2,5-acid chloride, THF, Et_3N, 12 h, reflux (70–80 %); iv) $POCl_3$, reflux, 17 h (60–70 %); v) Lawesson's reagent, toluene, reflux, 17 h (40–50 %).

Results and Discussion

Synthesis and characterization

The synthetic route is elucidated in Scheme 1. Common methodologies for the synthesis were same as reported elsewhere.[11] Alkoxyethyl benzoates **5a**–**d** were prepared by using the Williamson's ether synthesis. Alkylation of ethyl-3,4-dihydroxy benzoate gave compound **5a**. Ethyl-3,5-dihydroxy benzoate was *O*-alkylated to give compound **5b**, whereas alkylation of ethyl-3,4,5-trihydroxy benzoate gave compounds **5c** and **5d**. On treatment with hydrazine hydrate, these esters gave respective hydrazides **4a**–**d**, which were treated with thiophene-2,5-diacid chloride under basic conditions to give the corresponding hydrazides (**3a**–**d**). These hydrazides were treated with phosphoryl chloride to give the corresponding dioxadiazoles (**1a**–**d**) or with Lawesson's reagent to give the thiadiazole derivatives (**2a**–**d**). A molecular structural characterization was carried out by using ^1H and ^{13}C NMR spectroscopy, IR spectroscopy, and MALDI-TOF mass spectrometry (see the Supporting Information for details). The electron-withdrawing nature of the oxadiazole units compared with the thiadiazole units is reflected by the low-field ^1H NMR signals obtained for compounds **1a**–**d** with respect to compounds **2a**–**d** (see the Supporting Information). For example, the ^1H NMR spectrum of compound **1c** with two oxadiazole units showed low-field signals for protons H_a and H_b compared with those of compound **2c** with two thiadiazole units (Figure 1).

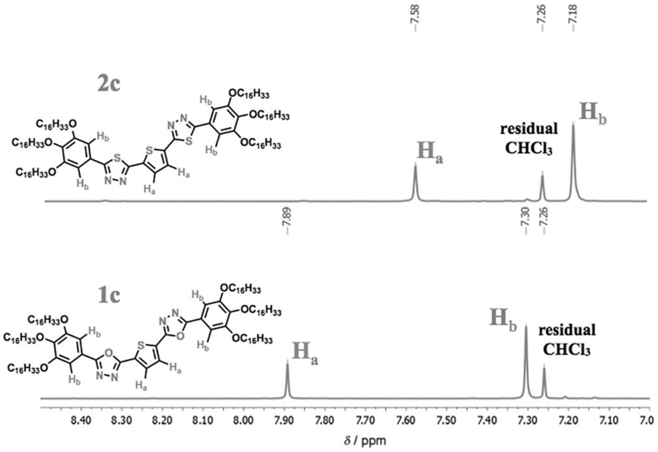

Figure 1. Overlay of the expanded portion of the ^1H NMR spectra ($CDCl_3$, 600 MHz) of **2c** and **1c**.

Thermal behavior

All the compounds were investigated by using thermogravimetric analysis (TGA), polarizing optical microscopy (POM), and differential scanning calorimetry (DSC). Polycatenars were stable up to at least 315 °C, except for compounds **1b** and **2b**. These compounds, which have alkoxy groups at the 3,5-positions, were stable only up to approximately 230 °C, as shown by the TGA results (Figure S36). The mesophase-type, phase-transition temperatures, and associated enthalpy changes are

Table 1. The phase-transition temperatures[a] and corresponding enthalpies of the polycatenars.

	Phase sequence					
	2nd heating			1st cooling		
	Phase[c]	T [°C]	E [kJ mol^{-1}]	Phase[c]	T [°C]	E [kJ mol^{-1}]
1 a	Cr	113.0	138.1	I	138.2	24.8
	Col$_{ob2}$	130.2	28.4	Col$_{ob1}$	129.3	27.3
	Col$_{ob1}$	138.1	25.4	Col$_{ob2}$	87.9	125.7
	I			Cr		
1 b	Cr$_1$	29.1	203.1	I	20.6	142.38
	Cr$_2$	73.5	124.1	Cr		
	Cr$_3$	77.3	129.4			
	I					
1 c	Col$_{r2}$	58.8	56.1	I	77	3.9
	Col$_{r1}$	65.7	127.07	Col$_h$	53.5	127.5
	Col$_h$	81.1	2.8	Col$_{r1}$	48.7	71.7
	I			Col$_{r2}$[b]		
1 d	Cr	24.24	28.7	I	75.4	10.3
	Col$_{ob}$	78.8	10.5	Col$_{ob}$	16.3	16
	I			Cr		
2 a	Cr$_1$	64.2	10.4	I	100.6	33.2
	Cr$_2$	101.3	19.8	Cr$_3$	91.2	99.3
	Cr$_3$	105.8	7.1	Cr$_2$	55.4	10.6
	Cr$_4$	125.8	17.9	Cr$_1$		
	I					
2 b	Cr	88.3	277.6	I	65.5	278.5
	I			Cr		
2 c	Col$_{r2}$	55.8	11.3	I	96.1	20.9
	Col$_{r1}$	59.7	65.4	Col$_{h1}$	90.9	25.4
	Col$_{h2}$	93	26.7	Col$_{h2}$	55.1	75.2
	Col$_{h1}$	97.2	20.2	Col$_{r1}$	48.1	10.9
	I			Col$_{r2}$[b]		
2 d	Col$_{h2}$	71.5	16.0	I	116.6	69.5
	Col$_{h1}$	120.5	71.6	Col$_{h1}$	67.4	15.8
	I			Col$_{h2}$[b]		

[a] Peak temperatures in the DSC thermograms obtained during the first heating and cooling cycles at 5 °C min^{-1}. [b] The mesophase freezes in glassy state and does not crystallize up to −20 °C. [c] Col$_{ob}$ = columnar oblique phase, Col$_r$ = columnar rectangular phase, Col$_h$ = columnar hexagonal phase, Cr = crystalline, I = isotropic.

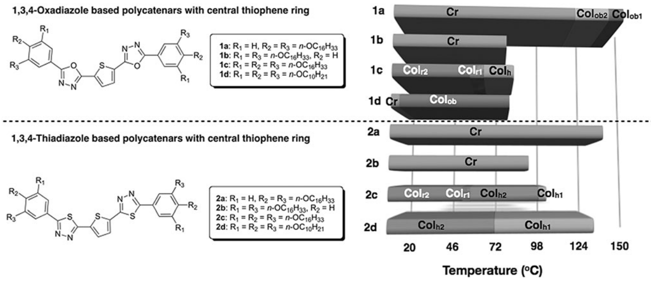

Figure 2. Bar graph summarizing the thermal behavior of **1 a**–**d** and **2 a**–**d** (second heating cycle); Col$_{ob}$ = Columnar oblique phase, Col$_r$ = columnar rectangular phase, Col$_h$ = columnar hexagonal phase.

presented in Table 1. Figure 2 graphically represents the thermal behavior of compounds in the second heating scans.

A crystalline sample of oxadiazole-based polycatenar **1 a**, with four hexadecyloxy tails connected to the terminal benzene rings at the 3,4-positions, exhibited enantiotropic mesomorphism; on heating, the crystalline sample showed a transition to a birefringent fluid at a temperature of approximately 113 °C, after passing through a few crystal-to-crystal transitions as observed in the DSC scans. The birefringent fluid was shearable and converted to an isotropic liquid at a temperature of about 138 °C. On cooling (5 °C min^{-1}), the isotropic liquid showed a transition to a birefringent texture comprised of a mosaic pattern interspersed with homeotropic domains (Figure 3 a). The mesophase existed up to 129 °C over a temperature range of 9 °C and then transformed into another mesophase, as shown by a sudden change in the birefringence accompanied by an enthalpy change in the DSC (Figure 3 b,c). This mesophase existed up to around 88 °C, and then crystallized as observed with a loss of shearability and change in the textural pattern. The XRD studies were carried out at two different temperatures, that is, 136 and 122 °C (Table 2). The XRD pattern obtained at 136 °C showed several peaks in the low-angle region with d spacings of 44.41, 42.34, 41.28, 40.36, and 36.12 Å, along with a diffuse peak at a wide angle with a d spacing of 4.61 Å. The wide-angle diffuse peak corresponds to the packing of flexible tails. The low-angle d spacings ($0 < 2\theta < 5°$) correspond to the Miller indices (02), (12), (20), (21), and (−12) of a columnar oblique (Col$_{ob}$) lattice. The lattice parameters derived from these reflections were found to be $a = 83.9$ and $b = 90.2$ Å with a tilt angle of $\gamma = 79.9°$. The XRD pattern obtained at 122 °C showed a complex diffraction pattern with many peaks at low angles, but they could be assigned to another Col$_{ob}$ phase with a tilt angle of $\gamma = 68°$, and the lattice parameters a and b were reduced to almost half compared with the high-temperature Col$_{ob}$ phase. The number of molecules in a unit cell (Z) was found to be 1.3. These two Col$_{ob}$ phases are denoted as Col$_{ob1}$ and Col$_{ob2}$.

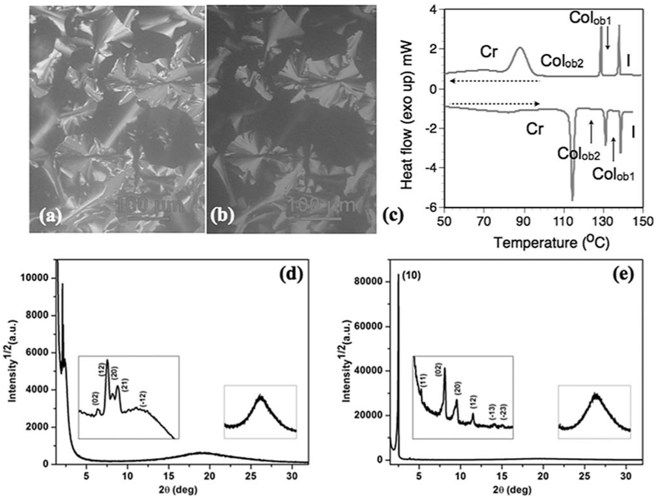

Figure 3. POM images of **1 a** a) at 132 (Col$_{ob1}$ phase) and b) 122 °C (Col$_{ob2}$ phase). c) DSC thermograms of **1 a** showing the first cooling (upper trace) and second heating (lower trace). XRD patterns obtained for **1 a** at d) 136 (Col$_{ob1}$ phase) and e) 122 °C (Col$_{ob2}$ phase).

Compound **1 b**, with four alkoxy tails connected to the terminal benzene rings at the 3- and 5-positions, proved to be crystalline, which shows the delicate balance involved in the LC self-assembly. Compound **1 c**, with six hexadecyloxy tails

Table 2. Results of indexation of XRD profiles of compounds **1 a**–**d**, at a given temperature (*T*) of the mesophase.[a]

Compound (*D* [Å])	Phase symmetry (*T* [°C])	d_{obsd} [Å][b]	d_{calcd} [Å][b]	Miller indices *hk*	Lattice parameters[c]
1 a (56.24)	Col_{ob1}, *P*2	44.41	44.41	02	$a=83.9$ Å
	(136)	42.34	42.34	12	$b=90.2$ Å
		41.28	41.28	20	$\gamma=79.9^\circ$
		40.36	40.24	21	
		36.12	36.53	−12	
		4.61(h_a)[d]			
	Col_{ob2}, *P*2	35.24	35.24	10	$a=38.0$ Å
	(122)	22.80	22.80	−11	$b=44.1$ Å
		20.44	20.44	02	$\gamma=68.0^\circ$
		17.83	17.62	20	
		15.29	15.36	−12	
		14.53	14.70	13	
		13.38	13.50	23	
		4.50 (h_a)[d]			
1 c (60.30)	Col_h, *P*6*mm*	35.47	35.47	10	$a=41$ Å
	(65)	20.53	20.48	11	
		4.48 (h_a)[d]			
	Col_{r2}, *P*2*mm*	37.63	37.63	01	$a=21.0$ Å
	(40)	21.00	21.00	10	$b=37.6$ Å
		18.28	18.33	11	
		13.64	14.01	12	
		4.20 (h_a)[d]			
		4.19 (h_c)[d]			
	Col_{r2}, *P*2*mm*	37.52	37.52	01	$a=21.0$ Å
	(25)	21.02	21.02	10	$b=37.5$ Å
		18.27	18.34	11	
		13.68	13.99	12	
		4.15 (h_a)[d]			
		4.17 (h_c)[d]			
1 d (45.35)	Col_{ob}, *P*2	33.78	33.78	01	$a=35.2$ Å
	(72)	33.01	33.01	11	$b=40.7$ Å
		29.24	29.24	10	$\gamma=56.1^\circ$
		4.50 (h_a)[d]			
		3.61 (h_c)[d]			
	Col_{ob}, *P*2	32.59	32.59	01	$a=34.4$ Å
	(50)	30.71	30.71	11	$b=37.2$ Å
		30.05	30.05	10	$\gamma=61.0^\circ$
		4.48 (h_a)[d]			
		3.59 (h_c)[d]			
	Col_{ob}, *P*2	32.09	32.09	11	$a=33.06$ Å
	(25)	31.18	31.18	01	$b=32.12$ Å
		15.57	15.57	12	$\gamma=76.1^\circ$
		4.41 (h_a)[d]			
		3.52 (h_c)[d]			

[a] The average diameter (*D*) of the polycatenars (estimated by using the Chem 3D Pro 8.0 molecular modeling software from Cambridge Soft). [b] d_{obsd} = observed spacing, d_{calcd} = calculated spacing (deduced from the lattice parameters; *a* and *b* for Col_{ob} and Col_r). [c] γ is the column tilt angle. [d] Spacings marked h_a and h_c correspond to diffuse reflections in the wide-angle region that arise from correlations between the alkyl chains and core regions, respectively.

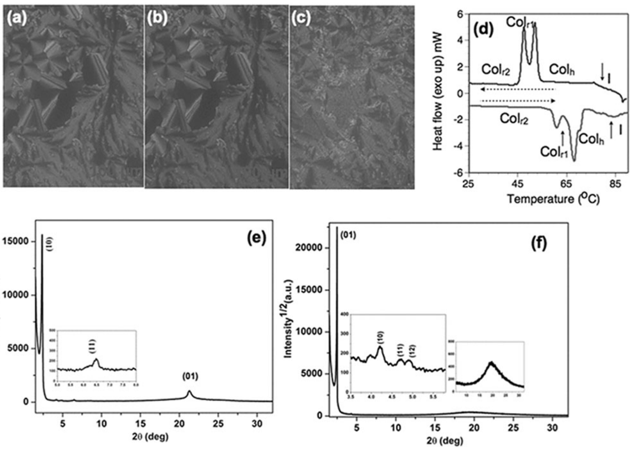

Figure 4. POM images of **1 c** at a) 65 (Col_h phase), b) 50 (Col_{r1} phase), and c) 28 °C (Col_{r2} phase). d) DSC thermograms of compound **1 c** showing first cooling (upper trace) and second heating (lower trace). XRD patterns obtained for **1 c** at e) 65 (Col_h phase) and f) 25 °C (Col_{r2} phase).

connected to the terminal benzene rings at the 3,4,5-positions, showed a mixture of pseudo-focal conic fans with mosaic patterns (Figure 4a) on slow cooling of the isotropic liquid at a rate of 5 °C min^{-1}. DSC scans during cooling showed transitions at approximately 54 ($\Delta H=127.5$ kJ mol^{-1}) and 49 °C ($\Delta H=71.7$ kJ mol^{-1}; Figure 4d). The first transition did not show a major difference in the optical texture, except for a decrease in the birefringence (Figure 4b), whereas the next transition showed the growth of a needle-like texture on the existing mosaic pattern (Figure 4c). This pattern remained unchanged up to room temperature. We carried out XRD studies at 65 and 40 °C and room temperature (Table 2). The diffraction pattern at 65 °C exhibited two sharp reflections at low angles with *d* spacings of 35.47 and 20.53 Å, along with a diffuse peak at wide angle with a *d* spacing of 4.48 Å. The first two *d* spacings in the low-angle region correspond to Miller indices (10) and (11) of a columnar hexagonal (Col_h) lattice. The lattice parameters were found to be $a=41$ Å. The spacing ratio is 1:0.578, which corresponds to a Col_h phase. The number of molecules derived from this lattice parameter in the unit hexagonal cell was found to be approximately 2. On cooling, this phase passed through a transition that spanned 5 °C, as seen in the DSC scans (Figure 4d), with a slight change in the color of the textural pattern. We could not carry out XRD studies in this short interval. The XRD studies carried out at 40 and 25 °C were almost identical. For example, the XRD pattern at 25 °C exhibited several peaks in the low-to-mid angle region with *d* spacings of 37.52, 21.02, 18.27, and 13.68 Å that corresponded to Miller indices (01), (10), (11), and (12) of a rectangular lattice. The spacing ratios were 1:0.56:0.49:0.36, which vary slightly from the spacing ratio in the higher-temperature XRD pattern obtained for Col_h phase. This could indicate the continuation of a higher-temperature Col_h phase. However, in view of the signatures from the DSC scans and a better agreement between the measured and calculated spacing values, we suggest that the lattices could be rectangular in nature. The wide-angle region showed two diffuse peaks at 4.15 and 4.17 Å. Here, the first peak corresponds to the packing of flexible alkyl tails, whereas the second diffuse peak originates from the stacking of the cores. There was not much change in the lattice parameters and the number of molecules within the rectangular unit cell. The number of molecules in a unit cell was found to be one irrespective of temperature. We denote this phase as Col_{r2}, whereas the phase present between Col_h and

Col$_{r2}$ that spans a thermal range of 5 °C is denoted as the Col$_{r1}$ phase because of the high enthalpy change associated with the phase transition from the high-temperature Col$_h$ phase (Figure 4a–c).

Compound **1d** with six *n*-decyloxy chains showed a mosaic texture on cooling from the isotropic liquid state, and the texture remained unchanged to room temperature (Figure S34a,b). This compound showed crystallization at 16 °C, as determined from the DSC cooling scan ($\Delta H = 16$ kJ mol^{-1}; Figure S34c). From the XRD studies, it was found that the Col$_{ob}$ phase was stabilized throughout the thermal range (Figure S34d,e). Thus polycatenars with shorter alkyl chains stabilized the Col$_{ob}$ phase, whereas polycatenars with longer alkyl chains (compound **1c**) stabilized the Col$_h$ and Col$_r$ phases.

The thermal behavior of the next series of polycatenars, in which the central thiophene ring was connected to two symmetrically substituted 1,3,4-thiadiazole rings, is discussed below. Compounds **2a** and **2b**, with four *n*-hexadecyloxy tails connected to the terminal benzene rings at the 3,4- and 3,5-positions, proved to be crystalline. On cooling from the isotropic temperature, hexacatenar **2c**, with six *n*-hexadecyloxy tails, showed a mosaic pattern interspersed with homeotropic domains, which is characteristic of a uniaxial phase (Figure 5a).

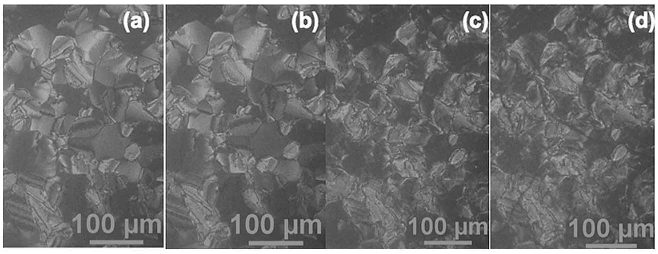

Figure 5. POM images of **2c** at a) 95 (Col$_{h1}$ phase), b) 88 (Col$_{h2}$ phase), c) 50 (Col$_{r1}$ phase), and d) 25 °C (Col$_{r2}$ phase).

At approximately 91 °C ($\Delta H = 25.4$ kJ mol^{-1}), a transition was observed in the DSC scan, whereas this change was very hard to detect in the POM (Figures 6a and 5b). The XRD pattern obtained at 90 °C shows two peaks at low angle with *d* spacings of 35.51 and 20.49 Å, along with two diffuse peaks at wide angle with *d* spacings of 4.58 and 3.7 Å (Table 3, Figure 6b). The first two low-angle peaks can be indexed to (10) and (11) reflections from a hexagonal lattice. The wide-angle spacings correspond to the packing of alkyl tails and the distance between the cores. The calculated lattice parameter *a* was 41 Å, which is 30% less than the molecular length (60.4 Å) of the polycatenar in the all-*trans* conformation. This difference indicates an intercalation of the peripheral tails of neighboring molecules in the Col$_h$ phase. We denote this columnar phase as Col$_{h2}$, whereas the one at higher temperature (> 91 °C) is denoted as the Col$_{h1}$ phase, based on the textural similarity. The number of molecules in the unit hexagonal cell was found to be two. This columnar phase spanned a thermal range of 36 °C before showing a textural change at approximately 48 °C, coupled with an enthalpy change of 104.9 kJ mol^{-1}. The XRD pattern obtained at 50 °C showed *d* spacings of 42.01, 25.63, 10.31, 5.77, 4.27, and 4.22 Å (Figure 6c). The relatively diffuse peak at 4.27 Å can be assigned to the packing of alkyl tails, whereas the other peaks correspond to Miller indices (01), (11), (31), and (45) of a rectangular lattice. The lattice parameters of the rectangular cell are $a = 32.3$ and $b = 42$ Å, with approximately two molecules ($Z = 1.9$) in the unit cell. We denoted this phase as Col$_{r1}$. The DSC scan showed a further transition at approximately 48 °C ($\Delta H = 38.5$ kJ mol^{-1}), whereas the texture remained same without showing signs of crystallization to room temperature. The XRD pattern obtained at room temperature (Figure 6d) exhibited additional reflections in the mid-angle region, but these reflections fit to a rectangular lattice and we denoted this phase as Colr$_2$. The two phases differ from each other with respect to the value of *a*. The Col$_{r2}$ phase shows a reduced value of *a*, whereas the value of *b* remains almost same.

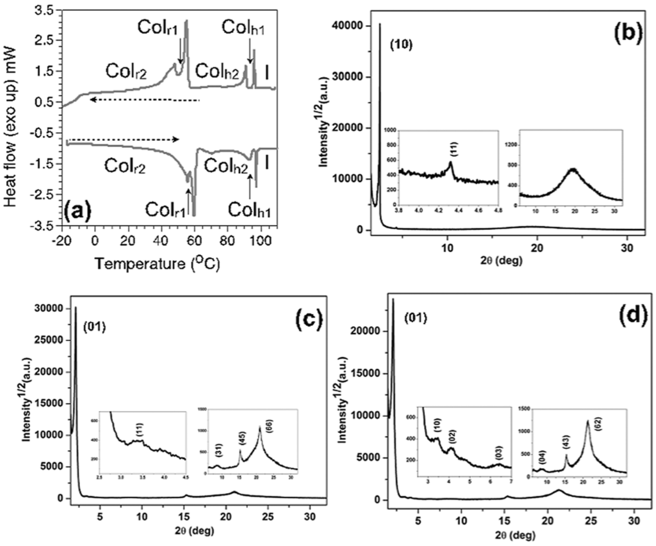

Figure 6. a) DSC thermograms of **2c** showing first cooling (upper trace) and second heating (lower trace). XRD patterns obtained for **2c** at b) 90 (Col$_{h2}$ phase), c) 50 (Col$_{r1}$ phase), and d) 25 °C (Col$_{r2}$ phase).

On cooling, the isotropic liquid of compound **2d**, which is the lower homologue of compound **2c** (with six *n*-decyloxy chains), showed the growth of spherulites that originated from the dark field of view (Figure S35a). Further cooling resulted in a transformation of these spherulites into a mosaic pattern at around 67 °C (Figure S35b), which remained unchanged to room temperature (Figure S35c). This transition was confirmed by the DSC scans, which showed an enthalpy change of 15.8 kJ mol^{-1} (Figure S35d, Table 1). There was no sign of crystallization up to −20 °C, as revealed by the DSC results. The XRD patterns obtained at 110, 60, and 25 °C confirmed a Col$_h$ phase (Figure S35e–g, Table 3). The DSC scans showed that there is a transition between two Col$_h$ phases, which we denoted as Col$_{h1}$, and Col$_{h2}$. It is surprising that the lower homologue exhibited a Col$_h$ phase in contrast to the oxadiazole analogue (**1d**), which exhibited a Col$_{ob}$ phase.

Looking at the thermal behavior, we can conclude that the length of the peripheral chain and pattern of substitution mat-

Table 3. Results of indexation of XRD profiles of compounds **2c–d**, at a given temperature (*T*) of the mesophase.[a]

Compound (*D* [Å])	Phase symmetry (T [°C])	d_{obsd} [Å][b]	d_{calcd} [Å][b]	Miller indices *hk*	Lattice parameters [Å]
2c (60.40)	Col$_{h2}$, *P6mm* (90)	35.51	35.51	10	$a=41.0$
		20.49	20.43	11	
		4.58 (h_a)[c]			
		3.70 (h_c)[c]			
	Col$_{r1}$, *P6mm* (50)	42.01	42.01	01	$a=32.3$
		25.63	25.63	11	$b=42.0$
		10.31	10.44	31	
		5.77	5.83	45	
		4.27 (h_a)[c]			
		4.22 (h_c)[c]			
	Col$_{r2}$, *P2mm* (25)	41.76	41.76	01	$a=25.6$
		25.60	25.60	10	$b=41.8$
		21.06	20.88	02	
		13.83	13.92	03	
		10.32	10.44	04	
		5.74	5.81	43	
		4.19 (h_a)[c]			
		4.17 (h_c)[c]			
2d (46.49)	Col$_{h1}$, *P6mm* (110)	29.82	29.82	10	$a=34.4$
		5.77 (h_a)[c]			
		4.34 (h_c)[c]			
	Col$_{h2}$, *P6mm* (60)	32.68	32.68	10	$a=37.7$
		16.38	16.34	20	
		11.74	12.35	21	
		5.78 (h_a)[c]			
		4.26 (h_c)[c]			
	Col$_{h2}$, *P6mm* (25)	32.52	32.52	10	$a=37.6$
		16.27	16.26	20	
		12.19	12.29	21	
		5.74 (h_a)[c]			
		4.18 (h_c)[c]			

[a] The average diameter (*D*) of the polycatenars (estimated by using the Chem 3D Pro 8.0 molecular modeling software from Cambridge Soft). [b] d_{obsd} = observed spacing, d_{calcd} = calculated spacing (deduced from the lattice parameters; *a* for Col$_h$, *a* and *b* for Col$_r$). [c] The spacings marked h_a and h_c correspond to diffuse reflections in the wide-angle region that arise from correlations between the alkyl chains and core regions, respectively.

ters in determining the thermal range of the mesophase. Oxadiazole derivative **1b** and thiadiazole-based polycatenar compound **2b** were crystalline in nature and showed that peripheral chain substitution at the 3,5-positions is not conducive for mesophase stabilization. This may be due to the lack of space filling and nanosegregation. Compound **1a**, with four peripheral alkyl chains substituted at the 3- and 4-positions of the terminal benzene ring, was liquid crystalline, whereas corresponding thiadiazole compound **2a** was crystalline, which indicated the effect of the thiadiazole ring on the self-assembly. Compounds **1c** and **2c** showed an enhanced mesophase range with respect to **1a**,**b** and **2a**,**b**, which showed that substitution at the 3,4, and 5-positions stabilized the columnar packing. Furthermore, a reduction in the length of the peripheral chain from *n*-hexadecyloxy to *n*-decyloxy (for compounds **1d** and **2d**) led to the broadest thermal range in the respective series. Oxadiazole derivatives **1a**, **1c**, and **1d** showed stabilized Col$_r$, Col$_h$, or Col$_{ob}$ phases, whereas thiadiazole derivatives **2c–d** exhibited Col$_r$ and Col$_h$ phases. Liquid crystallinity and the width of the mesophase exhibited by compounds **1a**, **1c**, **1d**, and **2c**, **2d** is a summation of bent-angle, dipole-moment, and space-filling effects and nanophase segregation. It is difficult to pinpoint a certain factor that establishes a relationship between the structure and the thermal behavior. This shows that a delicate ratio of incompatible subunits in a shape-anisotropic molecule is required to affect the nanophase segregation, which results in LC self-assembly. A general comparison of oxadiazole- and thiadiazole-based polycatenars based on a central thiophene leads to the following generalizations: Compounds with thiadiazole linkage show a rich phase sequence compared with oxadiazole derivatives. More importantly, the longer the chain length, the richer the phase sequence for both linking groups (oxadiazole or thiadiazole). For example, the higher (C16) homologue of the thiadiazole linking group (**2c**) shows a Iso–Col$_{h1}$–Col$_{h2}$–Col$_{r1}$–Col$_{r2}$ phase sequence, whereas the lower (C10) homologue (**2d**) has only two mesophases. Similarly, the C16 homologue of the oxadiazole linking group (**1c**) exhibits a Col$_h$ phase and two rectangular columnar phases, whereas the C10 homologue (**1d**) shows only the oblique columnar mesophase. A possible reason for this difference could be better isolation of the central cores in a columnar structure, provided by the longer peripheral chains.

Another point to be noted is that replacing a benzene ring with a thiophene ring leads to a richer mesophase scenario. We can compare the thermal behavior of these polycatenars (Figure 2) with previously reported polycatenars with a central benzene ring and substituted 1,3,4-oxadiazole[10c,d] or 1,3,4-thiadiazole[11b] as side rings. Figure 7 shows the phase-transition temperatures and mesophase widths of these polycatenars. To make a clear comparison, we chose the hexacatenar with *n*-decyloxy tails from each series. The bent angles of the central cores and other heterocycles help us to understand their impact on the self-assembly (Figure 8). The bent angle of polycatenars with a central benzene ring can be either 180 (for **p/10** and **pT/10**, *p*-substituted compounds) or 120° (for **m/10**

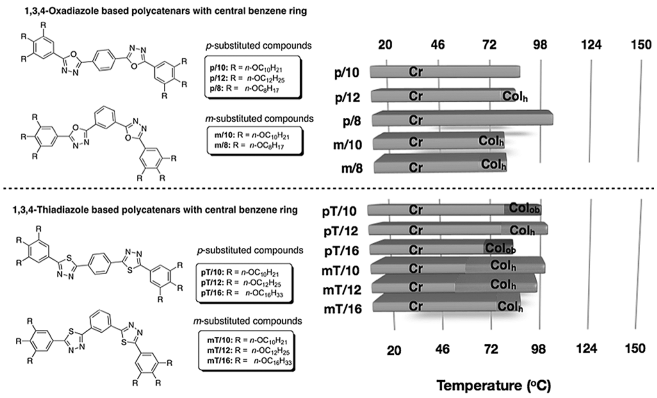

Figure 7. Bar graph summarizing the thermal behavior of 1,3,4-oxadiazole-based polycatenars[10c,d] with a central benzene ring substituted at the *p*- and *m*- positions and 1,3,4-thiadiazole-based polycatenars[11b] with a central benzene ring substituted at the *p*- and *m*- positions (second heating cycle); Col$_{ob}$ = columnar oblique phase, Col$_h$ = columnar hexagonal phase.

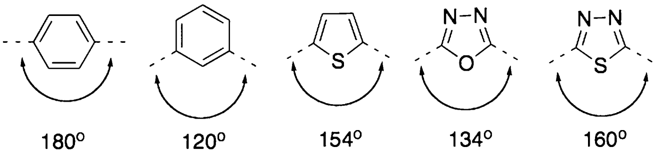

Figure 8. Comparison of the bent angles of different central and side rings of the polycatenars.[23]

and **mT/10**, *m*-substituted compounds). Here, for both series of oxadiazole- and thiadiazole-based polycatenars, *m*-substituted compounds show higher mesophase stabilization. Note that oxadiazole derivative **p/10** was crystalline, whereas **m/10** exhibited a Col_h phase. For the thiadiazole-based polycatenars, again the *m*-substituted compound **mT/10** showed a wider thermal range than *p*-substituted compound **pT/10**. Compared with polycatenars with oxadiazole side rings (bent angle ca. 134°), polycatenars based on thiadiazole side rings (bent angle ca. 160°) show higher mesophase stability. Therefore, an increase in the bent angle of the side rings helps to enhance the mesophase width.

Herein, the bent angle of the central thiophene ring is around 150°.[23] This is an intermediate angle compared with *p*- or *m*-substituted benzene. In this case, polycatenars with oxadiazole and thiadiazole side rings exhibited liquid crystallinity. The mesophase width is larger than *m*- and *p*-substituted polycatenars (both oxadiazole and thiadiazole) with a central benzene ring. It should be noted that, as in the case of benzene-centered polycatenars, thiadiazole-based polycatenar **2d** showed a wider thermal range than its oxadiazole counterpart (**1d**). Molecular models of hexacatenars with *n*-decyloxy chains are provided in the Supporting Information (Figure S42). This study confirms that this very small deviation in the bent angle (which is the effect of the hetero atom of the constituent rings in the polycatenar) leads to a huge difference in the self-assembly in the bulk. Smaller bent angles lead to a higher dipole moment, as in the case of oxadiazole derivatives, whereas larger bent angles reduce the overall dipole moment, as in the case of thiadiazole or thiophene derivatives. This also has a direct consequence on the mesophase stability. Another important factor is the bent angle provided by the central thiophene unit, which is very favorable for mesophase stabilization compared with previously reported benzene-centered polycatenars.

Photophysical studies

The photophysical properties of polycatenars **1a–d** and **2a–d** were investigated in the solution and thin-film states (Table 4). Absorption and emission spectra of these compounds were recorded for micromolar solutions in THF (Figure 9). As can be seen, the absorption spectra for the solutions of oxadiazole-based compounds **1a–d** showed absorption maxima in the range of $\lambda = 362$ to 365 nm (Figure 9a), whereas the thiadiazole-based compounds **2a–d** showed a slightly redshifted absorption spectrum at $\lambda = 368$ to 394 nm (Figure 9b). Oxadiazole derivatives **1a–d** showed higher bandgaps (3.07–3.2 eV) than thiadiazole derivatives **2a–d** (2.73–2.92 eV). Similarly, the emission maxima of compounds **1a–d** were in the range of $\lambda = 442$ to 476 nm, whereas the emission maxima of compounds **2a–d** were in the range of $\lambda = 476$ to 490 nm. Oxadiazole derivatives **1a–d** showed lower steady-state anisotropy values (0.071–0.088) than thiadiazole derivatives **2a–d** (0.122–0.142). The molar extinction coefficients of oxadiazole derivatives **1a–d** ($\varepsilon = 28\,800–31\,150\ \text{M}^{-1}\text{cm}^{-1}$) were found to be higher than thiadiazole derivatives **2a–d** ($\varepsilon = 20\,650–22\,900\ \text{M}^{-1}\text{cm}^{-1}$). The absorption bands mainly correspond to the π–π^* transition of this molecular system. Thin films of

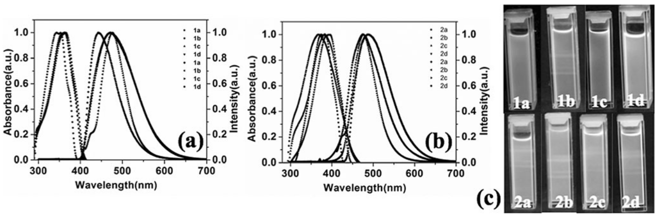

Figure 9. Absorption (solid trace) and emission (dotted trace) spectra of a) **1a–d** and b) **2a–d**. c) Photographs taken under UV light ($\lambda_{ex} = 365$ nm; micromolar solutions in THF).

Table 4. Photophysical properties in the solution and thin-film states.

	Solution state[a]							Thin-film state		
	Absorption [nm]	Emission [nm][b]	Stokes shift [nm]	λ_{onset} [nm]	$\Delta E_{g,opt}$[c] [eV]	Steady-state anisotropy	Relative quantum yield[d]	Absorption [nm]	Emission [nm][b]	Stokes shift [nm]
1a	365	442	77	405	3.07	0.087	0.72	365	473	108
1b	353	476	123	388	3.20	0.086	0.65	368	453	85
1c	362	472	110	405	3.07	0.088	0.57	367	478	111
1d	362	472	110	405	3.07	0.071	0.56	367	501	134
2a	368	476	108	455	2.73	0.130	0.50	373	486	113
2b	374	476	102	425	2.92	0.137	0.50	371	473	102
2c	383	487	104	455	2.73	0.142	0.54	365	512	147
2d	394	490	96	441	2.82	0.122	0.61	369	507	138

[a] As micromolar solutions in THF. [b] Excited at the respective absorption maxima; [c] Bandgap determined from the red edge of the longest wavelength (λ_{onset}) in the UV/Vis absorption spectra. [d] Standard: quinine sulfate in 0.1 M H_2SO_4.

these compounds showed small shifts in their absorption and emission spectra due to aggregation. Oxadiazole-based compounds **1a**–**d** showed higher quantum yields of 0.56 to 0.72, whereas thiadiazole-based compounds **2a**–**d** exhibited slightly lower quantum yields in the range of 0.5 of 0.61 (Figure S37). The observed quantum yields are higher in comparison to polycatenars with a central benzene ring instead of thiophene.[11b]

The thin films of these compounds were prepared by drop casting micromolar solutions of these compounds in toluene onto glass slides. The absorption spectra and emission spectra of these compounds were found to be broad compared with their solution spectra (Figure 10). The absorption spectra of the thin films of oxadiazole-based compounds **1a**–**d** show a redshift compared with the solution spectra; even though the absorption maximum of compound **1a** in the thin film shows the same value as in solution, the difference spectra shows the redshift (Figure S38; Figure 10a). Other than compound **1b**, the emission spectra of **1a**, **1c**, and **1d** showed a redshift (Figure 10b). In the case of thiadiazole-based compounds, all the compounds exhibited blueshifted absorption spectra except for compound **2a** (Figure 10d). The emission spectra of the films of thiadiazole derivatives **2a** and **2c**–**d** showed a redshift, whereas that of compound **2b** was blueshifted (Figure 10e). All the compounds showed a visually perceivable bright emission in the thin-film state on irradiation with long-wavelength UV light (Figure 10c,f).

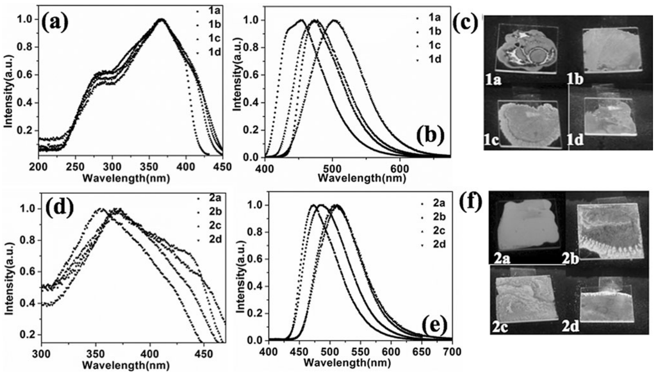

Figure 10. a) Absorption and b) emission spectra of **1a**–**d** and d) absorption and e) emission spectra of **2a**–**d**. c,f) Photographs of thin films of **1a**–**d** and **2a**–**d** taken under UV light ($\lambda_{ex} = 365$ nm).

It is evident from previous reports that the redshifted absorption spectra in the aggregated state points to the formation of J-type aggregates,[14] in which the molecules are arranged in a slipped-stack position, whereas the blueshifted absorption spectra indicates the formation of H-type aggregates, in which the molecules are arranged in a cofacial manner. J-aggregates are supposed to be highly luminescent compared with H-aggregates, in which luminescence is quenched. However, there are a few reports of fluorescent H-type aggregates.[15] Here we cannot provide conclusive proof of the formation of a particular type of aggregate in the thin films because of the possibility of several diastereomeric conformations for these polycatenars.

The photophysical properties of representative compounds **1c** and **2c** were studied in solution with different solvents to examine their behavior with different solvent polarities (Figure 11, Table 5). The absorption spectra did not vary much with respect to solvent polarity, which indicates the nonpolarity of the molecules in the ground state. In contrast to the absorption spectra, the emission spectra showed a redshift, which indicates the polar nature of the excited state. The presence of donor and acceptor moieties in conjugation leads to the localization of π electrons towards the acceptor unit in polar solvents. This leads to an internal charge-transfer state in addition to the locally excited state. The internal charge-transfer state is affected by solvent polarity. Thus the energy gap between the ground and excited states is reduced in polar solvents, which leads to a redshifted emission.

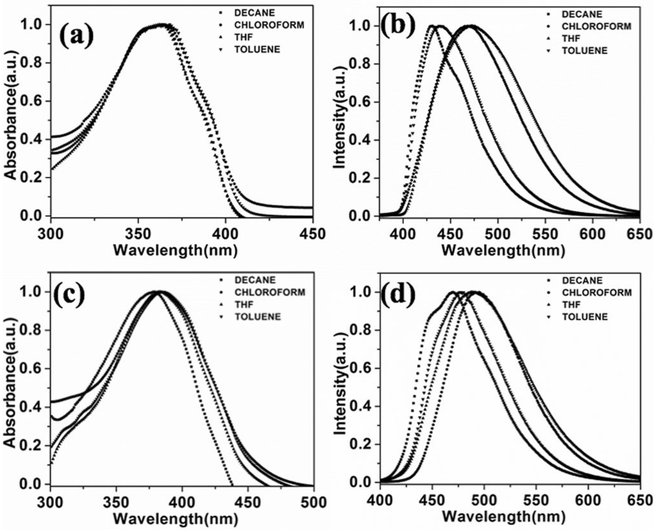

Figure 11. a) Absorption and b) emission spectra of **1c** (20 μmol) in different solvents and c) absorption and d) emission spectra of **2c** (20 μmol) in different solvents.

Table 5. Photophysical properties in different solvents.[a]

	Solvent	Absorption [nm]	Emission [nm][b]	Stokes shift [nm]
1c	decane	362	431	69
	toluene	362	438	76
	chloroform	362	468	106
	THF	362	472	110
2c	decane	379	470	91
	toluene	386	477	91
	chloroform	386	495	101
	THF	383	487	112

[a] As micromolar solutions in decane, toluene, chloroform, or THF. [b] Excited at the respective absorption maxima.

Electrochemical studies

Energy levels of frontier molecular orbitals (HOMO and LUMO) of the polycatenars were obtained by using cyclic voltammetry (CV) and the data are tabulated in Table 6. All the compounds exhibited irreversible oxidation and reduction waves (see Figure S39). The optical band gap ($E_{g,opt}$) was estimated from the red edge of the absorption spectra. Energy levels of the LUMO and HOMO were determined by using the formulae $\Delta E_{CV} = E_{LUMO} - E_{HOMO}$, $E_{HOMO} = -(4.8 - E_{1/2,Fc,Fc^+} + E_{ox,onset})$, and $E_{LUMO} = -(4.8 - E_{1/2,Fc,Fc^+} + E_{red,onset})$. Compounds **1a**–**d** exhibited LUMO levels of −3.04 to −3.21 eV and HOMO levels of −5.95 to −6.11 eV. Compounds **2a**–**d** exhibited LUMO levels of −3.17 to −3.31 eV and HOMO levels of −5.90 to −5.96 eV. Oxadiazole derivatives **1**–**d** exhibited a higher bandgap of 3.07 to 3.2 eV compared with thiadiazole derivatives **2a**–**d**, which showed a bandgap of 2.73 to 2.92 eV. Compounds **2a**–**d** can be compared with polycatenars reported previously, in which the central benzene ring is connected to thiadiazole rings at the 3,5-positions.11b These compounds show reduced LUMO, HOMO levels and bandgaps compared with their benzene analogues.

Table 6. Electrochemical properties.[a,b]

	E_{1red} [V][d]	E_{1ox} [V]	E_{HOMO} [eV][c]	E_{LUMO} [eV][d]	ΔE_{CV} [eV][e]	$\Delta E_{g,opt}$ [eV][f]
1a	−1.16	1.61	−5.95	−3.18	2.77	3.07
1b	−1.30	1.74	−6.08	−3.04	3.04	3.20
1c	−1.06	1.77	−6.11	−3.28	2.83	3.07
1d	−1.13	1.66	−6.00	−3.21	2.79	3.07
2a	−1.04	1.60	−5.94	−3.30	2.64	2.73
2b	−1.13	1.61	−5.95	−3.21	2.74	2.92
2c	−1.03	1.56	−5.90	−3.31	2.59	2.73
2d	−1.17	1.62	−5.96	−3.17	2.79	2.82

[a] As micromolar solutions in dichloromethane. [b] Experimental conditions: Ag/AgNO$_3$ as the reference electrode, glassy carbon as the working electrode, platinum rod as the counter electrode, TBAP (0.1 M) as the supporting electrolyte, RT, scanning rate 0.05 mV s^{-1}. [c] Estimated from the onset oxidation peak values by using the formula $E_{HOMO} = -(4.8 - E_{1/2,Fc,Fc^+} + E_{ox,onset})$. [d] Estimated from the onset reduction peak values by using $E_{LUMO} = -(4.8 - E_{1/2,Fc,Fc^+} + E_{red,onset})$; $E_{1/2,Fc,Fc^+} = 0.46$ V. [e] Estimated from the formula $\Delta E_{CV} = E_{LUMO} - E_{HOMO}$. [f] Bandgap determined from the red edge of the longest wavelength in the UV/Vis absorption spectrum.

Gelation studies

Compounds **1c** and **2c** were investigated for their ability to undergo organogelation in solution in hexane, decane, dodecane, hexadecane, chloroform, dichloromethane, ethanol, dimethylsulfoxide (DMSO), *n*-butanol, tetrahydrofuran, benzene, toluene, and *m*-xylene. Both of these compounds showed gelation in hydrocarbon solvents, such as hexane, decane, dodecane, and hexadecane (Table S1). We also checked the gelation of other compounds in decane (Table 7). Compounds **1b**, **2a**, **2b**, and **2d** precipitated after being dissolved in decane, whereas compound **1d** dissolved in decane. Of the oxadiazole derivatives, **1a** and **1c** showed gelation whereas for the thiadiazole derivatives none of the compounds except **2c** showed gelation in decane. Oxadiazole-based compound **1a**, with four alkyl tails, showed gelation at a very low critical gel concentration (CGC) of 0.45 wt.%. This compound was gelated within 6 min after heat-assisted dissolution. Immediately after adding the compound to decane, the suspension was heated to obtain a clear solution. The resultant solution was allowed to cool for 10 minutes to form a gel at room temperature. Gel formation was confirmed by using the "stable to inversion of the glass vial" method, that is, the gel was unable to flow on inversion of the container, which confirmed the formation of a stable gel. Oxadiazole-based compound **1c**, with six alkoxy tails, showed a CGC of 1 wt.% and took longer to gelate (approximately 3 h), whereas thiadiazole-based compound **2c** (again with six alkyl tails) took almost 50 min from the point of complete dissolution with a CGC of 0.7 wt.% respectively. Therefore, compounds **1a** and **2c** qualify as supergelators because they are able to gelate at a very low CGC, that is, well below 1 wt.%.[16] All the gels were opaque and fluorescent (Figure 12a). Compound **1a** showed the ability to form self-standing and moldable gels of any given shape (Figure 12b). It is apparent that the gelation depends on a very delicate balance of the number and pattern of substitution of alkyl tails and the type of heterocycle present in the polycatenar.

Table 7. Gelation behavior and CGCs of **1a**–**d** and **2a**–**d** in decane.

	Properties[a]	CGC [wt.%][b]	T_{gel} [°C][c]
1a	G(O)	0.45	63
1b	P	–	–
1c	G(O)	1.00	71
1d	S	–	–
2a	P	–	–
2b	P	–	–
2c	G(O)	0.70	47
2d	P	–	–

[a] G = stable gel, P = precipitate, I = insoluble, S = soluble, O = opaque. [b] The critical gelation concentration is the minimum concentration necessary for gelation. [c] T_{gel} is the thermal stability of the gels.

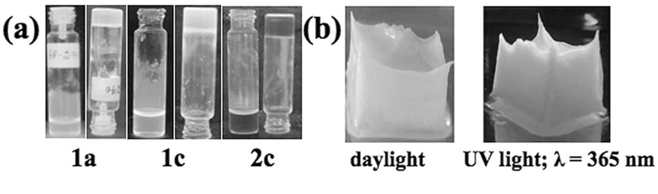

Figure 12. a) Photographs of **1a**, **1c**, and **2c** in the solution and gel states under long-wavelength UV light (λ = 365 nm) at the CGC. b) Formation of a self-standing gel of compound **1a** at the CGC.

Because we were interested in deriving the structure–property relationships, we decided to investigate compounds **1c** and **2c** by using extensive photophysical studies, microscopy, and XRD studies. Detailed rheological measurements were also carried out on the two representative samples, as described below. Formation of the organogel was monitored by measuring the emission spectra of the solution with respect to temperature and time. For compound **1c** the emission intensity increased as the temperature was decreased from 70 to 20 °C, with a concomitant redshift from $\lambda = 461$ to 471 nm (Figure 13). A huge fourfold increase in the emission intensity was observed on gelation, compared with the solution-state emission (5.51 mM in decane; Figure 14a). Similarly, the intensity of the emission was highest at 115 min and thereafter remained steady (Figure 13d). This is a phenomenon of aggregation-induced enhanced emission (AIEE). The emission spectra showed a redshift upon gelation (Figure 13c), which was similar to the observation in Figure 13b. This gel formation was reversible for many cycles of heating and cooling, as shown by the change in the emission intensity at its emission maximum (Figure 14b).

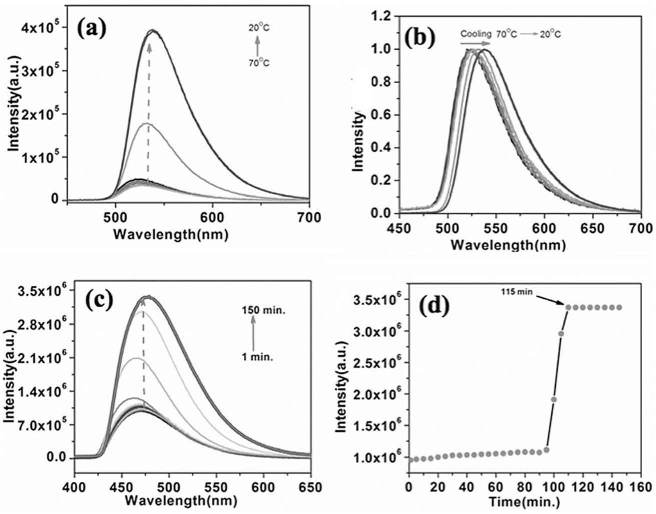

Figure 13. a) Emission spectra showing an increase in the emission intensity with a decrease in temperature from solution to the gel state for **1c**. b) Normalized emission spectra of **1c**, showing a redshift on gelation. c) Emission spectra showing an increase in the emission intensity with time during the transformation from solution to gel. d) Plot showing the change in emission intensity at the emission maximum ($\lambda = 362$ nm) vs. time (concentration: 5.51 mM, decane).

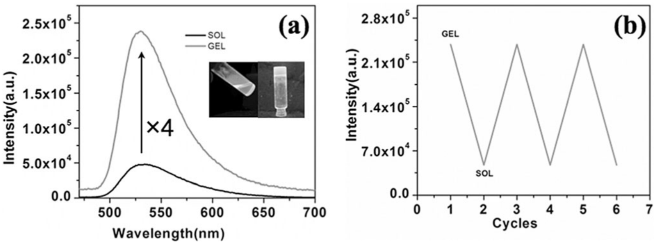

Figure 14. a) The increase in intensity from the solution state to gelation, showing aggregation-induced emission for **1c** at the CGC. b) Reversible change in the emission intensity at $\lambda = 362$ nm on repeated sol–gel transitions (concentration: 5.51 mM, decane).

Compound **2c** exhibited similar behavior. An increase in the emission intensity and a redshift in the emission was observed upon gelation (Figure 15a–b. The increase in emission intensity upon gelation from solution at the CGC (3.8 mM, decane) was found to be fivefold, which confirmed the AIEE phenomenon (Figure 16a). From solution to the gel state, a redshift was observed from $\lambda = 520$ to 538 nm. The gelation process, monitored by fluorescence spectroscopy with respect to time and temperature, showed similar behavior (Figure 15). The gelation was complete in 45 min and the intensity of the emission remained steady (Figure 15d). Similar to **1c**, the gel formation was reversible over many cycles of heating and cooling (Figure 16b).

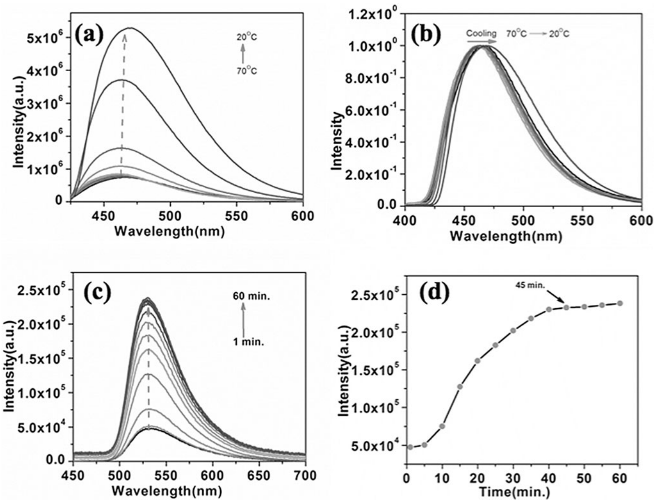

Figure 15. a) Emission spectra showing an increase in the emission intensity with the decrease in temperature from solution to the gel state for **2c**. b) Normalized emission spectra of **2c**, showing a redshift on gelation. c) Emission spectra showing an increase in the emission intensity with time during the transformation from solution to gel. d) Plot of the change in emission intensity at the emission maximum ($\lambda = 383$ nm) vs. time (concentration: 3.8 mM, decane).

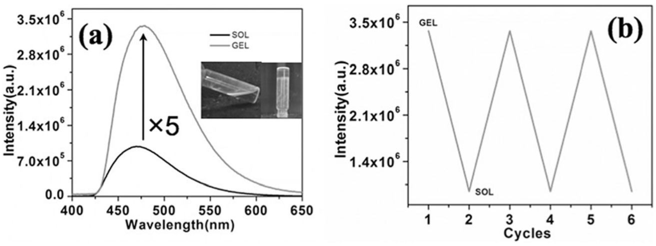

Figure 16. a) The increase in intensity from the solution state to gelation, showing aggregation-induced emission for **2c** at the CGC. b) Reversible change in the emission intensity at $\lambda = 383$ nm on repeated sol–gel transitions (concentration: 3.8 mM, decane).

Fluorescence lifetimes of the excited species formed in very dilute (20 µM) or concentrated (5.51 mM) solutions of **1c** in decane (at CGC) were measured by monitoring at the emission maxima ($\lambda = 472$ nm for the dilute solution and $\lambda = 471$ nm for the concentrated solution). The solution with lower concentration showed monoexponential decay with a single excited species ($T_1 = 1.05$ ns (100%)). The solution with higher concentra-

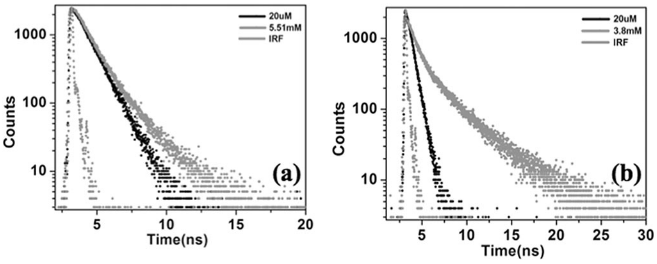

Figure 17. a) The fluorescence decay of **1c** in decane; IRF is the instrument-response function; $\lambda_{exc}=375$ nm. b) The fluorescence decay of **2c** in decane; $\lambda_{exc}=375$ nm.

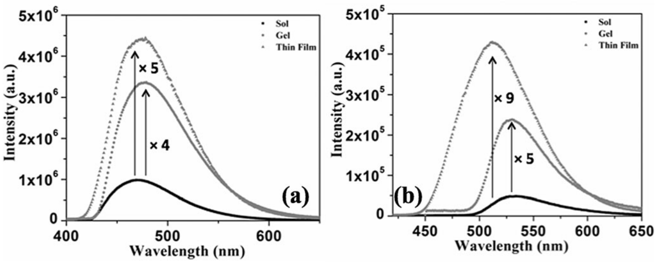

Figure 18. a) Emission spectra of **1c** in solution, gel (5.51 mM, decane), and thin-film states and b) emission spectra of **2c** in solution, gel (3.8 mM, decane), and thin-film states.

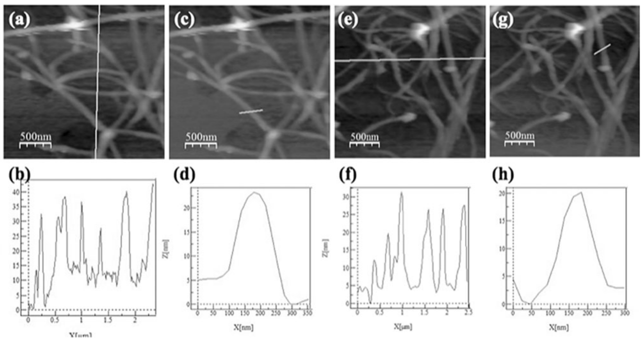

Figure 19. a), c) AFM images obtained for the xerogel of **1c** obtained from a 5.51 mM solution in decane (scale bar 0.5 μm). b) Expanded region of (a) showing the height profiles of the individual fibers and d) expanded region of (b) showing the thickness of an individual fiber. e), g) AFM images obtained for the xerogel of **2c** obtained from a 3.8 mM solution in decane (scale bar 0.5 μm). f) Expanded region of e) showing the height profiles of the individual fibers and h) expanded region of (g) showing the thickness of an individual fiber.

tion showed the presence of two excited-state species, one with a higher lifetime ($T_1=1.6$ ns (49%)) and the other with a lower lifetime ($T_2=0.93$ ns (51%); Figure 17a). Similar behavior was observed for **2c**. The fluorescence lifetimes of the excited species formed in the 20 μM and 5.51 mM solutions of **2c** in decane were measured by monitoring at their emission maxima ($\lambda=487$ nm for the dilute solution and $\lambda=538$ nm for the concentrated solution). The 20 μM solution showed a single species ($T_1=0.55$ ns (100%)). The solution at higher concentration exhibited biexponential decay with two species. One species showed a lower lifetime ($T_1=0.57$ ns (22%)), which can be attributed to the solvated monomer, whereas the other showed a higher lifetime ($T_2=3.79$ ns (78%)), which is due to aggregation (Figure 17b). We measured the excitation spectra of **1c** and **2c** at 20 μM and also at their CGC. The excitation spectra of **1c** at the gelation concentration showed a large blueshift compared with the excitation spectra obtained for the 20 μM solution. For compound **2c**, a slight redshift was observed with associated broadening of the excitation spectrum (Figure S40). An additional band was also observed at lower wavelengths. This shows that although the aggregation takes place in both compounds, the extent and nature of aggregation is different in each compound. The blueshifted excitation spectra of **1c** hint at the formation of H-aggregates. For compound **2c**, both blueshifted and slightly redshifted bands are present in the excitation spectra, which corresponds to the formation of both H- and J-aggregates, with the latter being the major product.[14,22]

At this point, we were curious to compare the emission of the LC aggregates in the thin films and gels of **1c** and **2c**. An overlay of the emission spectra of these compounds in the solution, gel, and thin-film states showed that the emission intensity of the LC thin films was quite high compared with the solution and gel states (Figure 18). It is surprising to see that the thin film of **1c** exhibited fivefold-enhanced emission (Figure 18a), whereas **2c** exhibited ninefold-enhanced emission with respect to the solution state (Figure 18b). From an application point of view, this is of high technological importance in emissive displays.

These gels were further characterized extensively through atomic force microscopy (AFM; Figure 19) and scanning electron microscopy (SEM; Figure S41). The AFM microscopic images of the xerogels of **1c** and **2c** show entangled networks of fibers. The fibers found in the xerogels were several micrometers in length, with an average height of 30 to 40 nm and an average thickness of around 150 nm. The SEM images of the xerogels of **1c** and **2c** also show similar entangled networks of fibers.

POM of the xerogels of **1c** and **2c** show a birefringent pattern as shown in Figure 20, inset, which suggests the presence of anisotropic order (Table 8). Therefore, a powder XRD study of the xerogel was carried out to investigate the structure of this self-assembly. The XRD pattern of the xerogel of **1c** shows several peaks at low angles that can be indexed to the Col_r phase with lattice constants $a=26.5$ and $b=36.5$ Å (Fig-

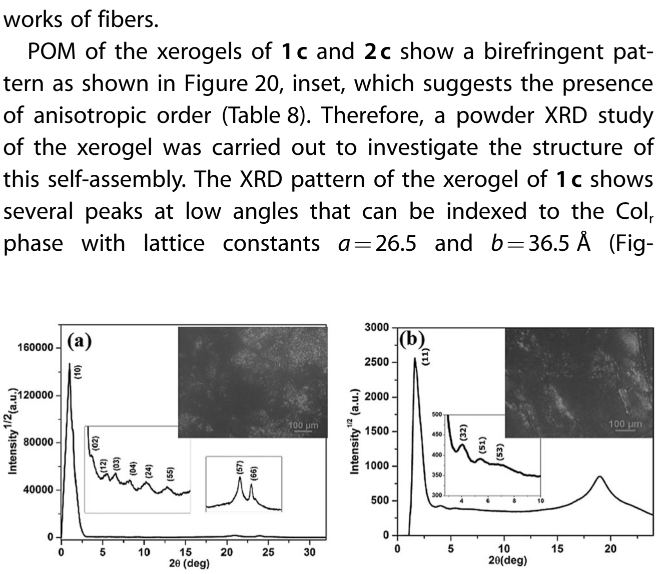

Figure 20. a) XRD patterns obtained for the xerogel of **1c** (Col_r phase); inset: the obtained POM image of **1c**. b) XRD patterns obtained for the xerogel of **2c** (Col_h phase); inset: the obtained POM image of **2c**.

Table 8. Results of indexation of XRD profiles of xerogels of **1 c** and **2 c** at RT.

Compound (D [Å])	Phase	d_{obsd} [Å]	d_{calcd} [Å]	Miller indices *hk*	Lattice parameters [Å]
1 c (60.3)	Col_r	26.5	26.5	10	$a = 26.5$
		18.3	18.3	02	$b = 36.5$
		15.1	15.0	12	
		12.0	12.2	03	
		9.6	9.1	04	
		7.7	7.5	24	
		4.2	4.3	55	
		3.7	3.7	57	
		3.5	3.6	66	
2 c (60.4)	Col_h	54.2	54.2	11	$a = 108.3$
		21.9	21.5	32	
		16.4	16.9	51	
		13.0	13.4	53	
		4.68			
		3.98			

ure 20 a, Table 8). The presence of several peaks in the low- and mid-angle regions suggested higher intercolumnar order in the columnar self-assembly. Therefore, compound **1 c** forms a columnar self-assembly in LC and gel states. Similarly the *d* spacings obtained from the diffraction pattern (Figure 20 b) of the xerogel of **2 c** could be fitted to a Col_h phase with the lattice constant $a = 108.3$ Å. Thus the self-assembly of the two polycatenars in the LC and gel states is dependent on the type of hetero atom present in the adjacent rings of the thiophene moiety. This can be schematically represented as shown in Figure 21 a,b. Compound **1 c**, which is in the form of a discoid, self-assembles to form columns, and these columns further self-organize into a Col_h phase, which on further cooling forms a Col_r phase that is stable at room temperature. In the presence of a hydrocarbon solvent, the compound forms nanofibers of several micrometers in length, which further entangle to form a dense network of fibers that entrap a huge amount of solvent (Figure 21 a). In compound **2 c**, two molecules organize to form a disc that self-assembles to form columns, and these columns further self-organize into a Col_h phase. On cooling, the arrangement of columns changes to a rectangular lattice that is stable at room temperature. Interestingly, on interaction with the hydrocarbon solvent this compound forms nanofibers with the columns arranged in a hexagonal lattice, as revealed by the XRD studies (Figure 21 b). This shows the impact of an atomic-scale difference (< 2 % of the molecular weight) on the self-assembly of polycatenars in the gel state. It is also important to note that the long nanofibers are mainly formed by π–π interactions and can be termed as molecular nanowires with a central conductive core and a peripheral insulating sheath. This long-range self-assembly is helpful from the viewpoint of applications in organic electronic devices.

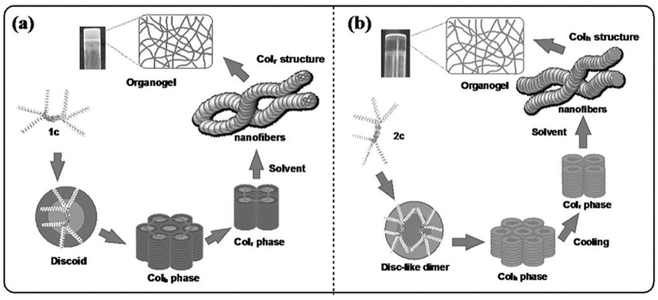

Figure 21. Diagram of the self-assembly of a) **1 c** and b) **2 c** in LC and gel states.

Rheological studies

To establish the elastic nature of the gel samples, dynamic rheological measurements that involved strain sweep, angular frequency sweep, and step-strain measurements were carried out. The dependence on the strain amplitude (γ) of the storage or elastic modulus (G') and loss or viscous modulus (G'') obtained for representative gels **1 c** and **2 c** is shown in Figure 22 a. At low γ values, both the samples show strain-independent behavior for G' and G'', with $G' > G''$. This solid-like behavior is typical of a gel structure.[17] Above a critical strain amplitude ($\gamma_c = 0.004$ for **2 c** and 0.03 for **1 c**), which defines the upper limit of the linear viscoelastic regime (LVR), both G' and G'' become strain-dependent. G' shows a monotonic decrease for both samples, whereas G'' for **2 c** passes through a maximum before decreasing. The latter feature is associated with soft glassy rheological (SGR) behavior[18] universally seen in materials such as foams, slurries, and pastes. The magnitude of G', a direct measure of the mechanical stiffness, was found to be lower and the LVR longer for **1 c**. These features indicate that although **2 c** is a stiff gel (higher G'), it is less robust than **1 c**. In both gels, G' crosses over G'' at higher γ values (above γ_c), which signals a deformation-driven transition from a viscoelastic solid to a viscoelastic liquid.[19] The variation in G' and G'' with angular frequency (ω) obtained by keeping the strain amplitude constant in the LVR is shown in Figure 22 b. Both G' and G'' show almost no variation with ω, with an elastic response ($G' > G''$) over the entire frequency range studied, which confirms the gel nature of the samples.[17] A further gel

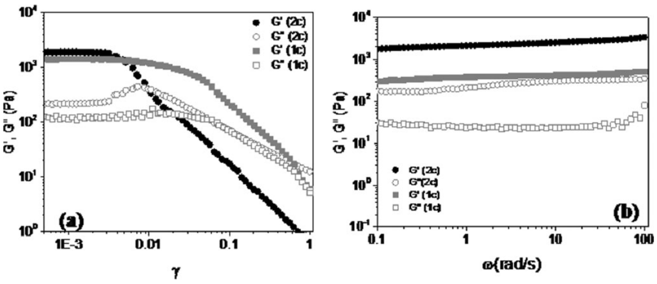

Figure 22. a) The dependence of storage (G') and loss (G'') moduli on strain (γ) for **1 c** and **2 c**. The temperature was kept constant at 20 °C and the angular frequency (ω) at 1 rad s^{-1}. b) Angular frequency (ω) vs. G' and G'' for **1 c** and **2 c**. The temperature was kept constant at 20 °C. The strain amplitude (γ) for both samples was kept constant at a value that corresponded to the LVR.

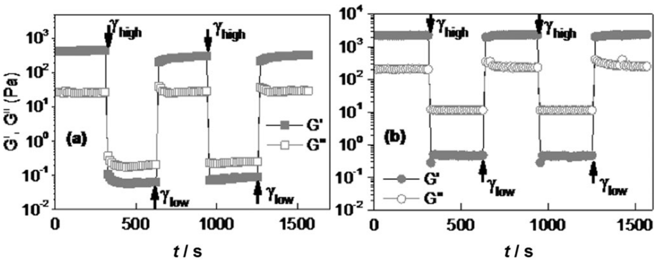

Figure 23. a) The step-strain with $\omega = 1$ rad s^{-1} for a gel of **1c** showing the collapse of the gel structure when the gel was subjected to a high oscillatory strain (γ) of 5 (regions indicated as high). On application of a γ of 0.001 (regions marked low), gel recovery took place within about 20 s and was reproduced over repeated cycles of measurement. b) The data obtained for the same experiment for **2c**.

collapse and recovery test was done by performing step-strain measurements (Figure 23). For this, the samples were subjected to a large amplitude strain ($\gamma > \gamma_c$), which resulted in the breakdown of the gel structure; subsequently, the strain was reduced to a smaller amplitude ($\gamma < \gamma_c$), with G' and G'' monitored throughout. The results obtained for **1c** (Figure 23a) show that on application of high γ, G' decreased by orders of magnitude and became smaller than G'', which resulted in a viscous state. When the strain was reduced to $\gamma < \gamma_c$, the elastic state was recovered. The gel collapse and recovery was found to be instantaneous, with a response time of less than 20 s, and was reproducible over repeated cycles of measurement, which indicated the mechanical robustness of both samples.[19]

In the steady-state measurements the shear viscosity (η) was determined as the samples were subjected to increasing shear rate ($\dot{\gamma}$). The obtained flow curves (η vs. $\dot{\gamma}$) are shown in Figure 24a,b for **2c** and **1c**, respectively. Although both samples show an overall shear-thinning behavior, **2c** exhibits an anomaly in the data that gives rise to three distinct regions. In region I at low shear rates, the viscosity decreased as the shear rate was increased, which is typical shear-thinning behavior. In region II, η started increasing as $\dot{\gamma}$ was increased and exhibited a shear-thickening behavior. This unusual behavior is indicative that structural changes are taking place in the gel, and needs extensive optorheological measurements to explain the phenomena. Similar flow behavior has been observed in triblock-copolymer-decorated systems in which region II (termed the transition region) corresponds to the coexistence of lamellar and onion phases.[20] On further increasing the shear rate, the shear-thinning behavior reappeared (region III). Regions I and III both show a power-law behavior with an identical exponent of 0.8 ± 0.06, which is lower than the power-law exponent (0.95 ± 0.01) obtained for **1c**. The neat shear-thinning behavior of **1c** with increased shearing conditions makes it more suitable for applications that require uniform spreadability.[21]

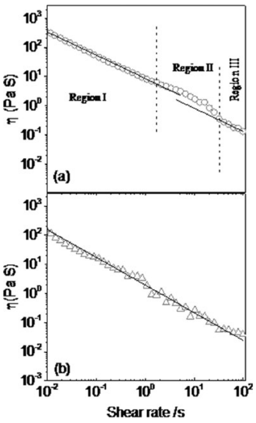

Figure 24. The dependence of viscosity (η) on shear rate for a) **2c** and b) **1c**. Whereas **1c** exhibits simple shear-thinning behavior, **2c** shows an anomaly with regions I and III showing shear-thinning behavior and region II showing shear-thickening behavior.

Conclusion

Two series of polycatenar mesogens that contain a central thiophene moiety connected to two substituted oxadiazole or thiadiazole units have been prepared. These heterocycles are connected to peripherally substituted phenyl groups. The number, length, and position of substitution of the peripheral chains were varied. The oxadiazole-based polycatenars exhibited a columnar phase with rectangular and hexagonal or oblique symmetry, whereas thiadiazole-based polycatenars exhibited columnar phases with rectangular and/or hexagonal symmetry. All the compounds exhibited bright emission in the solution and thin-film states. Two oxadiazole-based molecules and one thiadiazole-based molecule exhibited good ability to undergo gelation in hydrocarbon solvents at very low concentrations, which qualifies them as supergelators. The supergelation is mainly supported by attractive π–π interactions, along with other weak forces. Of these gels, the oxadiazole- and thiadiazole-containing hexacatenars with *n*-hexadecyloxy chains were studied extensively. These gels showed aggregation-induced enhanced emission, which is of high technological importance for applications in solid-state emissive displays. X-ray diffraction studies showed that the fibers of the xerogels formed by oxadiazole-based polycatenars self-assembled in a rectangular columnar phase, whereas those of the thiadiazole-based polycatenars self-assembled in a hexagonal columnar phase. The number, length, and position of substitution of the peripheral tails and the type of heterocycle moiety adjacent to the thiophene ring greatly affected the self-assembly of the molecules in the LC and gel states. Rheological measurements carried out on the samples confirmed the formation of gels quantitatively and showed that these gels are mechanically robust. The shear-rate dependence of bulk viscosity exhibited an overall shear-thinning behavior, with the exception of an anomaly of shear thickening at a smaller range of shear rates in one of the gels studied. The impact of an atomic-scale difference (oxygen to sulfur, < 2% of the molecular weight) on the self-assembly and the macroscopic properties of these self-assembled compounds have been clearly visualized. This molecular design helps in the development of long molecular nanowires with a strong overlap of central conducting cores and an insulating peripheral sheath, which will be helpful for applications in organic electronic devices.

Acknowledgements

A.A.S. sincerely thanks the Science and Engineering Board (SERB), DST, Govt. of India, and BRNS-DAE for funding this work through project no. SB/S1/PC-37/2012 and no. 2012/34/

31/BRNS/1039, respectively. We thank the Ministry of Human Resource Development for Centre of Excellence in FAST (F. no. 5-7/2014-TS-VII). We thank Monika Gupta and Dr. Santanu Kumar Pal from IISER Mohali for providing the XRD data for xerogel **2c**.

Keywords: columnar phases · gels · liquid crystals · polycatenars · self-assembly

[1] a) A. Mishra, C.-Q. Ma, P. Bäuerle, *Chem. Rev.* **2009**, *109*, 1141 – 1276; b) M. Melucci, L. Favaretto, A. Zanelli, M. Cavallini, A. Bongini, P. Maccagnani, P. Ostoja, G. Derue, R. Lazzaroni, G. Barbarella, *Adv. Funct. Mater.* **2010**, *20*, 445 – 452; c) K. Takimiya, S. Shinamura, I. Osaka, E. Miyazaki, *Adv. Mater.* **2011**, *23*, 4347 – 4370; d) I. F. Perepichka, D. F. Perepichka, *Handbook of Thiophene-Based Materials*, Wiley-VCH, Weinheim, **2009**.

[2] a) J. Zaumseil, H. Sirringhaus, *Chem. Rev.* **2007**, *107*, 1296 – 1323; b) J. L. Brusso, O. D. Hirst, A. Dadvand, S. Ganesan, F. Cicoira, C. M. Robertson, R. T. Oakley, F. Rosei, D. F. Perepichka, *Chem. Mater.* **2008**, *20*, 2484 – 2494; c) J. Shi, Y. Li, M. Jia, L. Xu, H. Wang, *J. Mater. Chem.* **2011**, *21*, 17612 – 17614.

[3] a) I. F. Perepichka, D. F. Perepichka, H. Meng, F. Wudl, *Adv. Mater.* **2005**, *17*, 2281 – 2305; b) X. Jiang, Z. Zheng, Y. Harima, J. Ohshita, P. Sun, *J. Mater. Chem.* **2011**, *21*, 1902 – 1906.

[4] a) S. Roquet, R. M. De Bettignies, P. Leriche, A. Cravino, J. Roncali, *J. Mater. Chem.* **2006**, *16*, 3040 – 3045; b) Y. Li, Y. Zou, *Adv. Mater.* **2008**, *20*, 2952 – 2958; c) T. H. Kwon, V. Armel, A. Nattestad, D. R. Macfarlane, U. Bach, S. J. Lind, K. C. Gordon, W. Tang, D. J. Jones, A. B. Holmes, *J. Org. Chem.* **2011**, *76*, 4088 – 4093; d) P.-L. T. Boudreault, A. Najari, M. Leclerc, *Chem. Mater.* **2011**, *23*, 456 – 469.

[5] a) D. Byron, A. Matharu, R. Wilson, G. Wright, *Mol. Cryst. Liq. Cryst.* **1995**, *265*, 61 – 76; b) R. Azumi, G. Götz, P. Bäuerle, *Synth. Met.* **1999**, *101*, 544 – 545; c) M. Funahashi, F. Zhang, N. Tamaoki, *Adv. Mater.* **2007**, *19*, 353 – 358.

[6] a) T. Yasuda, K. Kishimoto, T. Kato, *Chem. Commun.* **2006**, 3399 – 3401; b) T. Yasuda, T. Shimizu, F. Liu, G. Ungar, T. Kato, *J. Am. Chem. Soc.* **2011**, *133*, 13437 – 13444.

[7] Q. Li, Self-Organized Organic Semiconductors: From Materials to Device Applications; John Wiley & Sons: New York, **2011**.

[8] a) X. Li, A. Liu, S. Xun, W. Qiao, X. Wan, Z. Y. Wang, *Org. Lett.* **2008**, *10*, 3785 – 3787; b) K. B. Woody, B. J. Leever, M. F. Durstock, D. M. Collard, *Macromolecules* **2011**, *44*, 4690 – 4698; c) Y. Zhou, Y. Xiao, S. Chi, X. Qian, *Org. Lett.* **2008**, *10*, 633 – 636.

[9] a) Y. Shirota, *J. Mater. Chem.* **2000**, *10*, 1 – 25; b) D. Apreutesei, G. H. Mehl, *J. Mater. Chem.* **2007**, *17*, 4711 – 4715.

[10] a) J. Han, *J. Mater. Chem. C* **2013**, *1*, 7779 – 7797; b) B. Roy, N. De, K. C. Majumdar, *Chem. Eur. J.* **2012**, *18*, 14560 – 14588; c) J. Tang, R. Huang, H. Gao, X. Cheng, M. Prehm, C. Tschierske, *RSC Adv.* **2012**, *2*, 2842 – 2847; d) X. Yang, H. Dai, Q. He, J. Tang, X. Cheng, M. Prehm, C. Tschierske, *Liquid Crystals* **2013**, *40*, 1028 – 1034.

[11] a) S. K. Pathak, R. K. Gupta, S. Nath, D. S. S. Rao, S. K. Prasad, A. S. Achalkumar, *J. Mater. Chem. C* **2015**, *3*, 2940 – 2952; b) S. K. Pathak, S. Nath, R. K. Gupta, D. S. S. Rao, S. K. Prasad, A. S. Achalkumar, *J. Mater. Chem. C* **2015**, *3*, 8166 – 8182.

[12] a) V. Coropceanu, J. Cornil, D. A. da Silva Filho, Y. Olivier, R. Silbey, J.-L. Brédas, *Chem. Rev.* **2007**, *107*, 926 – 952; b) S. Prasanthkumar, A. Gopal, A. Ajayaghosh, *J. Am. Chem. Soc.* **2010**, *132*, 13206 – 13207; c) S. S. Babu, V. K. Praveen, A. Ajayaghosh, *Chem. Rev.* **2014**, *114*, 1973 – 2129.

[13] A. P. Sivadas, N. S. S. Kumar, D. D. Prabhu, S. Varghese, S. K. Prasad, D. S. S. Rao, S. Das, *J. Am. Chem. Soc.* **2014**, *136*, 5416 – 5423.

[14] a) F. Würthner, T. E. Kaiser, C. R. Saha-Moller, *Angew. Chem. Int. Ed.* **2011**, *50*, 3376 – 3410; *Angew. Chem.* **2011**, *123*, 3436 – 3473; b) F. Würthner, C. Bauer, V. Stepanenko, S. A. Yagai, *Adv. Mater.* **2008**, *20*, 1695 – 1698; c) F. Würthner, C. Thalacker, S. Diele, C. Tschierske, *Chem. Eur. J.* **2001**, *7*, 2245 – 2253.

[15] a) D. D. Prabhu, N. S. S. Kumar, A. P. Sivadas, S. Varghese, S. Das, *J. Phys. Chem. B* **2012**, *116*, 13071 – 13080; b) M. Kasha, H. R. Rawls, M. A. El-Bayoumi, *Pure Appl. Chem.* **1965**, *11*, 371 – 392; c) F. C. Spano, *Acc. Chem. Res.* **2010**, *43*, 429 – 439.

[16] a) R. Yoshida, *Adv. Mater.* **2010**, *22*, 3463 – 3483; b) A. Harada, R. Kobayashi, Y. Takashima, A. Hashidzume, H. Yamaguchi, *Nat. Chem.* **2011**, *3*, 34 – 37; c) T. Yamamoto, M. Yoshida, *Langmuir* **2012**, *28*, 8463 – 8469; d) M. Zhang, D. Xu, X. Yan, J. Chen, S. Dong, B. Zheng, F. Huang, *Angew. Chem. Int. Ed.* **2012**, *51*, 7011 – 7015; *Angew. Chem.* **2012**, *124*, 7117 – 7121; e) K. Yuichiro, T. Yoshinori, H. Akihito, Y. Hiroyasu, H. Akira, *Sci. Rep.* **2013**, *3*, 1243.

[17] S. B. Ross-Murphy, *J. Rheol.* **1995**, *39*, 1451 – 1463.

[18] a) P. Sollich, *Molecular gels, Materials with Self-assembled Fibrillar Networks*, Ed: R. G. Weiss and P. Terech, Springer the Netherlands **2006**; b) H. M. Wyss, K. Miyazaki, J. Mattsson, Z. Hu, D. R. Reichman, D. A. Weitz, *Phys. Rev. Lett.* **2007**, *98*, 238 – 303.

[19] G. G. Nair, S. K. Prasad, R. Bhargavi, V. Jayalakshmi, G. Shanker, C. V. Yelamaggad, *J. Phys. Chem. B* **2010**, *114*, 697 – 704.

[20] S. Fujii, D. Mitusmasu, Y. Isono, W. Richtering, *Soft Matter* **2012**, *8*, 5381 – 5390.

[21] B. W. Barry, M. C. Meyer, *Int. J. Pharmacol.* **1979**, *2*, 1 – 25.

[22] a) Y. Deng, W. Yuan, Z. Jia, G. Liu, *J. Phys. Chem. B* **2014**, *118*, 14536 – 14545; b) D. D. Prabhu, A. P. Sivadas, S. Das, *J. Mater. Chem. C* **2014**, *2*, 7039 – 7046.

[23] a) K.-T. Lin, G.-H. Lee, C. K. Lai, *Tetrahedron* **2015**, *71*, 4352 – 4361; b) C. Selvarasu, P. Kannan, *J. Chem. Sci.* **2015**, *127*, 1831 – 1838; c) G. Shanker, M. Prehm, M. Nagaraj, J. K. Vij, M. Weyland, A. Eremin, C. Tschierske, *ChemPhysChem* **2014**, *15*, 1323 – 1335.

Received: August 2, 2016
Revised: September 2, 2016

FULL PAPER

Small difference, large impact: Two series of polycatenars composed of a central thiophene moiety substituted with either oxadiazole or thiadiazole units have been prepared. A detailed account of the impact of structural variations on liquid-crystalline and organogel self-assemblies is provided.

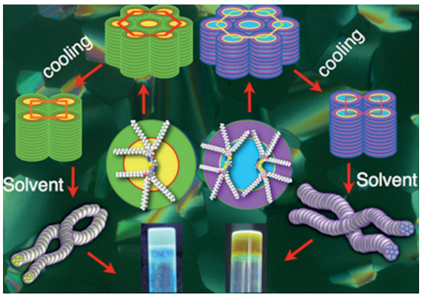

Liquid Crystals

*B. Pradhan, V. M. Vaisakh, G. G. Nair, D. S. S. Rao, S. K. Prasad, A. A. Sudhakar**

■■ – ■■

Effect of Atomic-Scale Differences on the Self-Assembly of Thiophene-based Polycatenars in Liquid Crystalline and Organogel States